Unsteady flow and mass transfer induced by Rayleigh-Bénard-Marangoni Convection

Jan Wissink, Fatima Ali and Herlina Herlina

Abstract Evaporative cooling at the water surface is usually modelled by imposing a constant heat flux at the surface. This boundary condition allows for variations in the water surface temperature T, which then induce variations in surface tension. The resulting Marangoni forces tend to move surface water from low surface tension (high T) regions to high surface tension (low T) regions. To study the combined effect of buoyancy and Marangoni forces on interfacial mass transfer, (fully resolved) direct numerical simulations have been performed. The simulations were carried out for a fixed macro Rayleigh number of $Ra_L = 21200$ and a variety of Marangoni (Ma) numbers to assess the relative importance of buoyancy and Marangoni forces on the air-water mass transfer. It is known that both forces tend to reinforce one another even though the underlying physical mechanisms are different. This is highlighted in the present results showing that Marangoni forces, acting at the water surface, induce very efficient mixing of dissolved gases (as well as heat) in a well-defined layer adjacent to the surface. Buoyant convection, on the other hand, tends to cause deep penetration of plumes of cold, saturated water into the bulk.

Jan Wissink
Brunel University London, Kinston Lane, Uxbridge UB8 3PH, UK,
e-mail: jan.wissink@brunel.ac.uk

Fatima Ali
Brunel University London, Kinston Lane, Uxbridge UB8 3PH, UK,
e-mail: fatima.ali2@brunel.ac.uk

Herlina Herlina
Karlsruhe Institute of Technology, Karlsruhe D76131, Germany,
e-mail: herlina@kit.edu

a

1 Introduction

The motivation behind this study is to gain a better understanding of the heat and mass transfer process across the air-water interface in natural water bodies. A specific example of this phenomenon is the heat and atmospheric gas transfer across the interface of lakes and reservoirs. It is vital to accurately predict the transfer rate in order to generate a definitive global heat and greenhouse gas budget. In this context, wind shear is commonly recognized as the primary factor responsible for generating turbulence, which supports the interfacial heat and mass flux [1], [2]. Typically, other sources of turbulence, such as buoyancy, are often overlooked. However, there has been a growing interest in buoyancy-driven heat and gas transfer resulting from surface cooling, especially in lakes and ponds with low wind speeds [3], [4], [5]. During this process, surface cooling, often caused by evaporation, leads to the formation of plumes and sheets of relatively dense, cold water. These cold-water (gas-saturated) plumes plunge down while being replaced by warmer bulk water that is not fully saturated, thus facilitating the heat and gas transfer across the water surface.

Surface cooling is known to create an unstable density gradient and can also cause variations in surface tension due to localized changes in temperature. These variations in surface tension give rise to Marangoni forces, which induce flows from regions of low surface tension (high temperature) to regions of high surface tension (low temperature). Consequently, buoyancy- and/or Marangoni-induced convective instabilities lead to the formation of convection cells at the surface [6], [7]. The characteristic pattern of these convection cells reveals the existence of one or more regions with elevated temperature within their structure [8]. Additionally, it demonstrates that individual cells are separated by narrow regions characterized by lower temperatures. Numerous theoretical and experimental studies have been conducted to explore the onset of the underlying instability and the resulting formation of convection cell patterns [9], [10], [11], [12]. Many of these investigations were motivated by applications in the field of chemical engineering and involved the utilization of a relatively thin fluid layer that was confined by a solid wall with a no-slip boundary condition. These studies demonstrated that within such thin fluid layers, horizontal temperature-gradient-induced Marangoni forces, in conjunction with buoyancy forces, promote the mixing of cooler surface water with warmer water from the upper bulk region [13], [14].

In previous numerical simulations of buoyancy-driven heat transfer across the air-water interface two approaches were commonly used: prescribing a constant temperature [8] or a constant heat flux [15], [16]. Unlike simulations where the surface temperature remains constant, constant-heat-flux simulations generate variations in surface temperature that results in the generation of Marangoni forces. It should be noted that in previous numerical investigations on the effect of these forces on interfacial mass transfer, the Marangoni forces were surfactant-concentration-induced [17], [18]. Even tiny amounts of surfactants were found to significantly inhibit interfacial mass transfer. Despite the potentially significant impact of Marangoni forces on heat

and mass transfer coefficients, the surface-temperature-induced ones were ignored in previous numerical studies.

Recently, a numerical study of the combined effect of buoyancy and Marangoni forces on developing interfacial heat transfer, was performed by Wissink and Herlina [19]. It was found that at a fixed Rayleigh number the Marangoni-force-induced-mixing of water from the surface and from the upper bulk resulted in a progressively earlier onset of the so-called Rayleigh-Bénard Marangoni (RBM) instability with increasing Marangoni number. Hence, it is to be expected that also the impact of Marangoni forces on interfacial mass transfer will be non-negligible.

In the paper we will present results of a series of fully resolved three-dimensional direct numerical simulations (DNS) that study the initial development of the RBM instability and its effect on interfacial mass transfer at a Rayleigh number of $Ra_L = 21200$ and a variety of Marangoni (Ma) and Schmidt (Sc) numbers. The results presented will show the development of convection cells from initially random disturbances added to the temperature field at $t = 10\,\mathrm{s}$, thereby highlighting the influence of Marangoni-forces on the instantaneous surface mass transfer velocity. Also, the effect of Marangoni forces on the scaling of the horizontally-averaged mass transfer K_L as a power of the Schmidt number will be investigated.

2 Numerical Aspects

The in-house numerical code employed was especially developed to produce fully resolved simulations of the subsurface flow and scalar fields. It allows for the application of a dual mesh, where the evolution of the velocity and temperature fields are calculated on the base mesh, while the evolution of the low-diffusivity scalars are calculated on a refined mesh. To normalise the components of the Navier-Stokes equations, the length scale $L = 0.01\,\mathrm{m}$ is used together with the velocity scale $U = \kappa/L\,\mathrm{m/s}$, where κ is the thermal diffusivity. As a result, using the Einstein summation convention, the continuity equation reads

$$\frac{\partial u_k}{\partial x_k} = 0 \tag{1}$$

and the momentum equations read

$$\frac{\partial u_i}{\partial t} + \frac{\partial u_i u_j}{\partial x_j} = -\frac{\partial p}{\partial x_i} + Pr\frac{\partial^2 u_i}{\partial x_j \partial x_j} + Ra_L\, Pr\, T^\star \delta_{i3} \;\; i = 1, \ldots, 3, \tag{2}$$

where u_1, u_2, u_3 are the normalised velocity components in the x_1, x_2, x_3 direction, respectively, with $x_1 = x, x_2 = y, x_3 = z$, p is the universal pressure, δ_{ij} is the Kronecker delta,

$$T^\star = \frac{T_{b,0} - T}{L(\partial T/\partial z)|_S} \tag{3}$$

is the nondimensional temperature, where $T_{b,0}$ is the intital temperature in the bulk, which is normalised using the heat flux at the surface and the length scale L (note that the subscript "S" denotes the water surface),

$$Ra_L = \frac{\alpha \, (\partial T/\partial z)|_S \, g L^4}{\kappa \nu} \tag{4}$$

is the Rayleigh number, where α is the thermal expansion rate, $g = -9.81\,\mathrm{m/s^2}$ is the gravitational acceleration, ν is the kinematic viscosity, and

$$Pr = \frac{\nu}{\kappa} = 7 \tag{5}$$

is the Prandtl number corresponding to a temperature of $T = 20°\mathrm{C}$. The Marangoni number, finally, is defined by

$$Ma_L = \frac{(\partial \sigma/\partial T) \, (\partial T/\partial z)|_S \, L^2}{\mu \kappa}, \tag{6}$$

where μ is the dynamic viscosity.

The scalar transport equations are solved in parallel with the Navier-Stokes equations. They consist of the convection-diffusion equations for the temperature

$$\frac{\partial T^\star}{\partial t} + \frac{\partial u_j T^\star}{\partial x_j} = \frac{\partial^2 T^\star}{\partial x_j \partial x_j}, \tag{7}$$

and the normalised scalar concentrations $C^\star = C/C_S$ (where C_S is the saturation concentration), given by

$$\frac{\partial C^\star}{\partial t} + \frac{\partial u_j C^\star}{\partial x_j} = \frac{Pr}{Sc} \frac{\partial^2 C^\star}{\partial x_j \partial x_j}, \tag{8}$$

where Sc is the Schmidt number defined by the ratio of the momentum diffusivity of the fluid and the mass diffusivity of the dissolved substance D.

2.1 Discretisations and Boundary Conditions

The discretisation of the momentum equations is carried out using fourth-order central discretisations of the convection and diffusion, while the Poison equation for the pressure is solved using the conjugate gradient method with diagonal preconditioning.

The convection-diffusion equations for the temperature and the normalised scalar concentrations $C^\star = C/C_S$ (where C_S is the saturation concentration) are solved using a fifth-order WENO scheme for the convection and a fourth-order central discretisation for the diffusion. The code is parallelised by dividing the computational

mesh in several blocks of identical size. Each block is allocated to a unique processing core, while communication between cores is done using the MPI protocol. The cubic computational domain, of size $5L \times 5L \times 5L$, is periodic in the horizontal directions. The surface is assumed to be flat with zero vertical velocity, fully saturated scalar concentrations and a fixed temperature flux to model evaporative cooling. The effect of Marangoni forces on the horizontal velocity components is modelled by

$$\begin{cases} \frac{\partial u}{\partial z} = -Ma_L \left.\frac{\partial T^\star}{\partial x}\right|_S \\ \frac{\partial v}{\partial z} = -Ma_L \left.\frac{\partial T^\star}{\partial y}\right|_S \end{cases}, \tag{9}$$

where the temperature derivatives are taken at the water surface. At the bottom, zero flux conditions are employed for all scalars in combination with a free-slip condition for the velocity.

2.2 Grid Resolution

In all simulations a $200 \times 200 \times 252$ mesh was used to discretise the $5L \times 5L \times 5L$ computational domain. In the horizontal directions the mesh was chosen to be uniform, while in the vertical direction the mesh was gradually refined towards the surface in order to resolve the thin thermal and concentration boundary layers.

Run	D1	D2	D3	D4	D5	D6	D7	D8	D9
Ma_L	−1050	−250	0	250	550	800	1050	2700	5250

Table 1 Overview of macro Marangoni numbers. In all simulations, $Ra_L = 21200$ and the refinement factor for the scalar mesh with $Sc = 50, 100, 200$ was $R = 2$.

In table 1 an overview is presented of the simulations discussed in this paper. All simulations employ the same Rayleigh number, $Ra_L = 21\,200$, combined with a variety of Marangoni numbers. The Prandtl number was set to $Pr = 7$ and the Schmidt numbers employed in the simultaneously solved scalar transport equations were $Sc = 50, 100, 200$. Note that all passive scalars were solved by refining the base mesh with a factor of 2, while the temperature was solved on the $200 \times 200 \times 252$ base mesh.

Figure 1 shows the maximum ratio over time of the geometric mean of the grid cell size

$$\overline{\Delta} = \sqrt[3]{\delta x \times \delta y \times \delta z}, \tag{10}$$

and the scaled horizontally-averaged Batchelor length scale at $Sc = s$ (or $Pr = s$)

$$\langle \pi \, \eta_{B,s} \rangle_{x,y}, \tag{11}$$

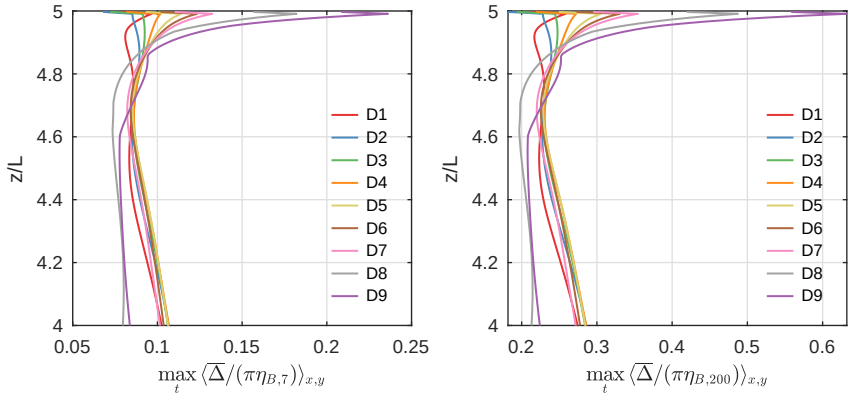

Fig. 1 Ratio of geometric mean of grid cells to (a) Batchelor scale at $Sc = 16$ (for base mesh) and (b) Batchelor scale at $Sc = 100$ (for two times refined mesh).

where $\delta x, \delta y, \delta z$ are the mesh sizes in the x, y, z-directions. It can be seen that in all simulations, the ratio $\overline{\Delta}/\langle \pi \, \eta_{B,s} \rangle_{x,y}$ is less than one for both $s = 7$ (resolved on the base mesh) and $s = 200$ (resolved on the two times refined mesh). Additionally (not shown here), in all simulations the linear (diffusive) part of the concentration boundary layer, located adjacent to the surface, is fully resolved by at least 4 grid points. Hence, according to the Grötzbach criterion, the scalar fields adjacent to the surface are sufficiently well resolved. Please note that for the convection part of the transport equations, a WENO scheme is used that is capable of resolving very steep gradients.

3 Results

The paper focuses on studying the mass transfer during the initial development of the RBM instability and the simulations were stopped some time after the first plumes started to fall down.

3.1 Instantaneous Mass Transfer

The RBM instability combines the effects of buoyancy forces and Marangoni forces. The former are responsible for the formation of thermal plumes that results from the accumulation of cold (relatively heavy) water near the surface. This process continues until sufficient potential energy is obtained to overcome diffusive forces resulting in cold water plumes penetrating relatively deep into the bulk. Marangoni

forces, on the other hand, result from local differences in surface tension, where a force is generated moving fluid from low surface tension (high $T|_S$) regions to high surface tension (low $T|_S$) regions. For a more detailed description see [19]. Both instabilities tend to reinforce one another even though the Marangoni forces only act at the surface and, hence, do not result in deep penetrative convection.

The surface heat flux continuously cools the instantaneous surface temperature $T|_S$, which results in an initial thickening of the thermal boundary layer. Simultaneously, also the concentration boundary layer thickens in time, which, in turn, results in a reduction of the instantaneous mass transfer velocity

$$k_L = \left| \frac{-1}{C - C_b} \frac{1}{Re\, Sc} \left. \frac{\partial C}{\partial z} \right|_S \right|. \tag{12}$$

Some time after the RBM instability starts to develop from the initially random disturbances, eventually $T|_S$ becomes increasingly non-uniform. In areas where the thermal boundary layer grows, generally also the concentration boundary layer becomes thicker so that k_L reduces. On the other hand, in areas where warm, unsaturated fluid from the (upper) bulk moves upwards both $T|_S$ and k_L become larger. Figure 2 illustrates the effect of the RBM instability in simulation D9 by comparing snapshots of the instantaneous surface temperature T and the instantaneous mass transfer velocity k_L at $Sc = 100$ for $t = 20, 28, 35, 58$ s, where the first two time-instances $t = 20, 28$ s correspond to the times where the horizontally-averaged k_L is minimum and maximum, respectively (see also figure 4). In this time-interval, increasingly well-defined convection cells can be seen to develop. Each convection cell consists of one or more upflow areas where relatively warm water from the lower thermal boundary layer flows to the surface, where it continues to flow in the radial direction as it cools down. At locations where two convection cells meet, the now relatively cold water is transported back down into the upper bulk. In time, the size of the convection cells can be seen to increase significantly. At $t = 20$ s, areas of low $T|_S$ can be seen to correlate well with areas of low k_L, while areas of high $T|_S$ correlate well with areas of high k_L. At later times, this correlation very gradually reduces. At $t = 58$ this deterioration can be seen most clearly. It is (partially) linked to an increased variation of k_L as reflected in the absence of k_L maxima in the middle of large convection cells (where peaks in T can clearly be observed) and the presence of local peaks of high instantaneous mass transfer in most of the smaller convection cells (which do correspond to peaks in $T|_S$). The peaks in the small convection cells are associated with small vortical structures immediately underneath the water surface that actively promote the local upflow of unsaturated, warm water from the lower thermal boundary layer resulting in the emergence of relatively small (often elongated) convection cells with a more intense mixing than in the larger cells). The emergence of these small surface-parallel) vortices are typical for the Marangoni instability and result in a locally increased vertical mixing.

Figure 3 shows snapshots from simulation D9 of the temperature T and the concentration C_{100} at $Sc = 100$ in the plane $y/L = 2.5$, taken at the same time instances as the snapshots of the instantaneous surface temperature and mass transfer

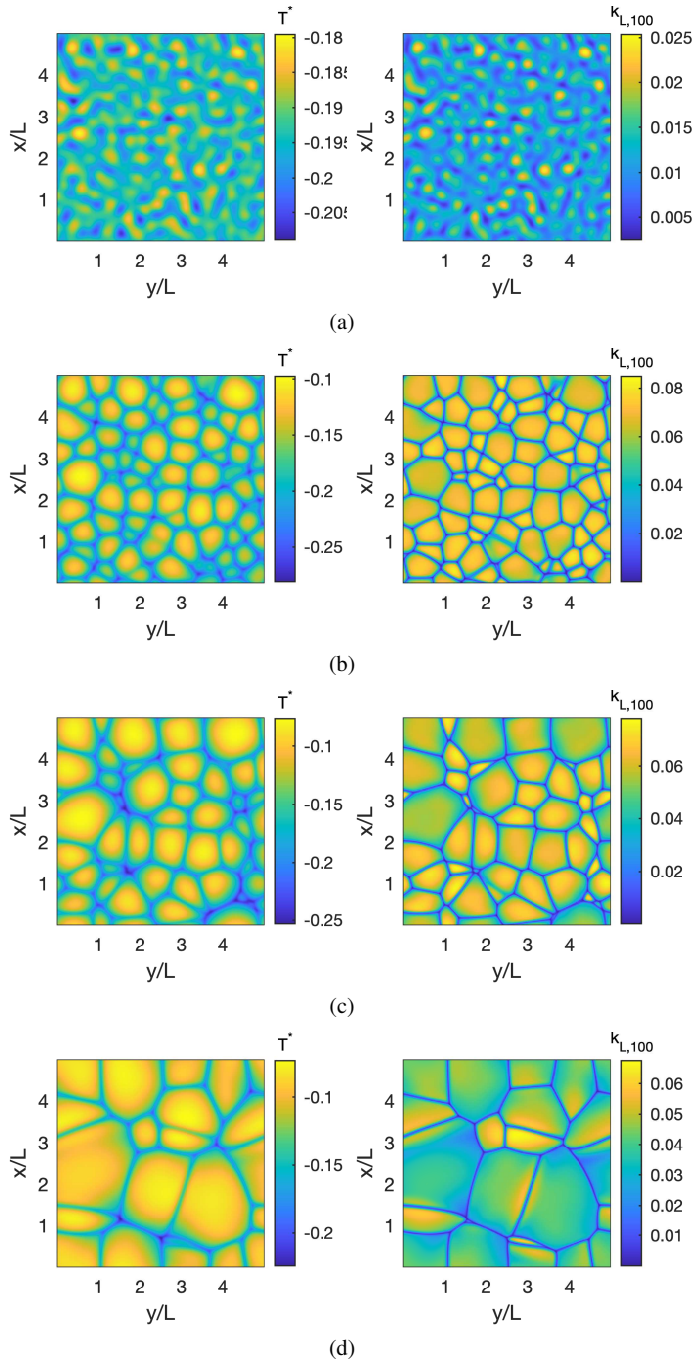

Fig. 2 Snapshots from simulation D9 of the instantaneous surface temperature and mass transfer velocity at $Sc = 100$ and (a) $t = 20$ s., (b) $t = 28$ s., (c) $t = 35$ s. and (d) $t = 58$ s.

in figure 2. It can be seen that at $t = 20\,\mathrm{s}$ the thermal boundary layer shows almost no disturbances (due to the relatively large thermal diffusivity with $Pr = 7$), while the concentration boundary layer at $Sc = 100$ shows very small disturbances. In time these disturbances grow and at $t = 28\,\mathrm{s}$ these disturbances also become clearly visible in the thermal boundary layer in the form of diffused thermal plumes. Because of the relatively high Schmidt number of $Sc = 100$, the concentration contours are much less diffused and clearly show the typical mushroom-shape that is often associated with the initial formation of thermal plumes driven by buoyant convection. In time, these plumes gradually merge such that their number reduces while their size increases. As a result, at $t = 58\,\mathrm{s}$ only two plumes remain visible in the plane $y/L = 2.5$, while due to significant differences in diffusion, the correlation between T and C_{100} gradually reduces.

3.2 Horizontally-Averaged Statistics

Figure 4 shows the development in time of the horizontally-averaged mass transfer velocity

$$K_L = \langle k_L \rangle_{x,y} \tag{13}$$

for all simulations D1-D9 listed in table 1. It can be seen that at a fixed Rayleigh number Ra_L, an increase in the Marangoni number results in an earlier onset of the RBM instability, as identified by K_L starting to deviate from its laminar value that is identified by the lower envelope of the curves (up to $t \approx 95\,\mathrm{s}$). While the positive Marangoni numbers used in simulations D4-D9 result in a promotion of the RBM instability, negative Marangoni numbers (simulations D1,D2) can be seen to progressively inhibit the RBM instability as the onset of growth in K_L is delayed compared to the purely buoyant simulation D3, where $Ma_L = 0$.

Figure 5 investigates (at a fixed $Ra_L = 21200$) the dependence of K_L/U on (a) Ma_L for $Sc = 50, 100, 200$ and (b) Sc for a variety of Marangoni numbers Ma_L at the time where K_L/U is maximum (see figure 4). In figure 5a, it can be seen that with increasing Schmidt number, not only K_L/U reduces for fixed Ma_L, but also that at each fixed Sc, the rate of increase in K_L/U with increasing Ma_L is reduced. Figure 5b indicates the existence of a power-law relation

$$\frac{K_L}{U} \propto Sc^n \tag{14}$$

for each fixed Marangoni number (with n dependent on Ma_L). For the purely buoyant simulation D3, with $Ma_L = 0$, the slope of $n = -0.49$ is very close to the theoretical slope of $n = -0.5$ obtained in [8], which is valid for simulations with a free-slip surface boundary condition for the velocity (such as obtained when $Ma_L = 0$). For $Ma_L \neq 0$, the slope n can be seen to noticeably deviate from -0.50. This is especially clear for larger Ma_L, where the slope gradually changes from $n \approx -0.50$ to $n = -0.40$ for simulation D9 with $Ma_L = 5250$.

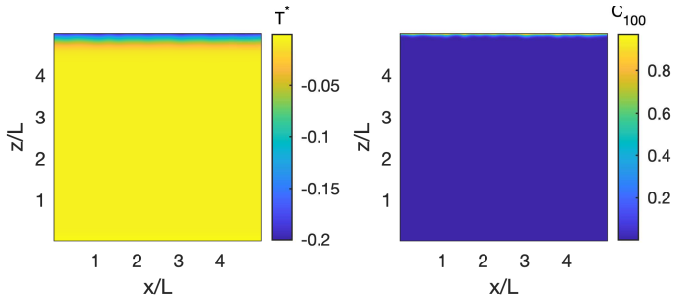

(a)

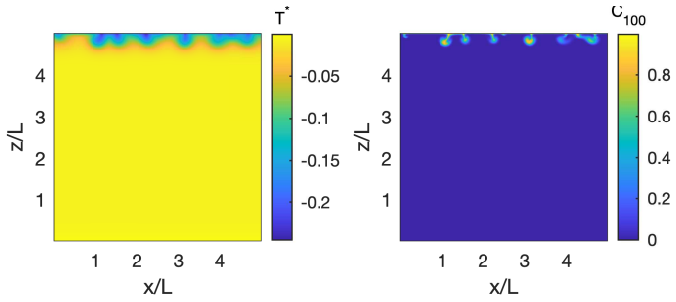

(b)

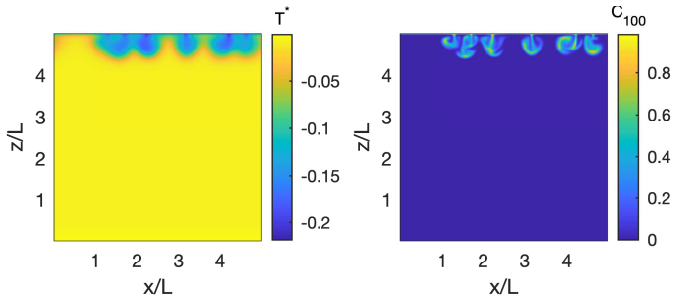

(c)

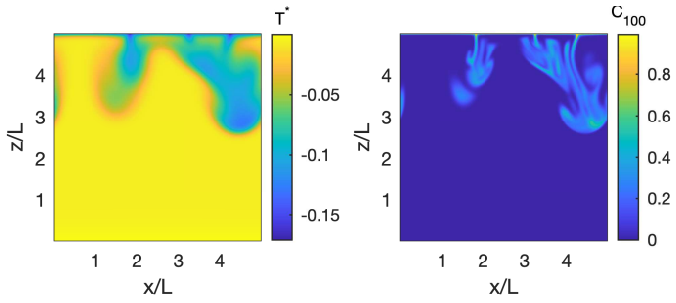

(d)

Fig. 3 Snapshots from simulation D9 of the instantaneous temperature T and concentration C_{100} at $Sc = 100$ and (a) $t = 20$ s., (b) $t = 28$ s., (c) $t = 35$ s. and (d) $t = 58$ s.

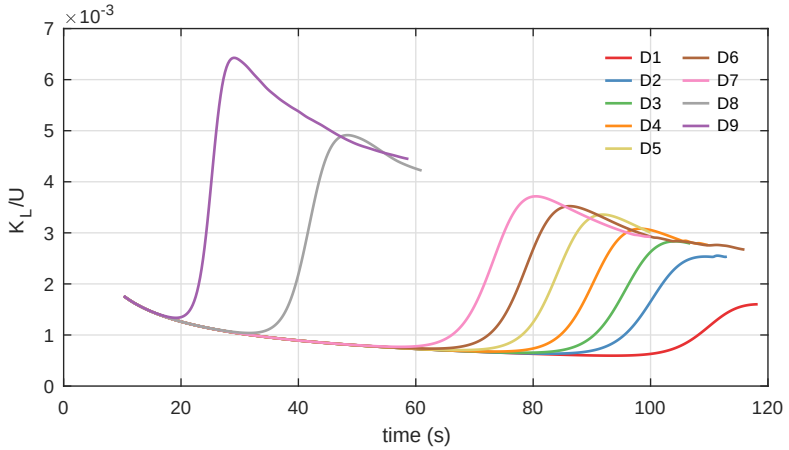

Fig. 4 Temporal evolution of K_L for various Marangoni numbers at fixed $Ra_L = 21200$ and $Sc = 100$.

In our previous work [18] it was shown that progressive damping of near surface turbulence leads to a gradual change of slope from $n = -0.5$ to $n = -2/3$ (corresponding to the value obtained for a no-slip surface boundary condition). Similarly, here it is also expected that a change in Ma_L from $Ma_L = 0$ to increasingly negative values of Ma_L will result in a similar change in slope n.

4 Conclusions

Fully resolved numerical simulations were performed to study interfacial mass transfer driven by an emerging Rayleigh-Bénard-Marangoni instability induced by employing a fixed surface heat flux to model evaporative cooling. The study focusses on the effect Schmidt and Marangoni numbers and uses a fixed Rayleigh number of $Ra_L = 21200$.

In our previous paper [19] it was shown that with increasing Ma_L, the speed at which the RBM instability develops significantly increases. It was also shown that, due to the fact that Marangoni forces act only at the surface, the (cold, saturated) fluid pushed down into the lower boundary layer by the Marangoni forces tends to linger close to the surface until sufficient cold fluid has accumulated for buoyancy forces to take charge and transport the saturated, cold fluid further down into the bulk. In this paper it was shown that the generation of shear by the presence of Marangoni forces caused a change in the scaling of the mass transfer velocity with Schmidt number, where the slope in the power law $K_L \propto Sc^n$ changes from $n \approx -0.50$ at $Ma_L = 0$ (free-slip condition) to $n = -0.40$ at $Ma_L = 5250$.

The combined effect of Rayleigh and Marangoni number on the above scaling is yet to be determined and will be the focus of a follow-up study.

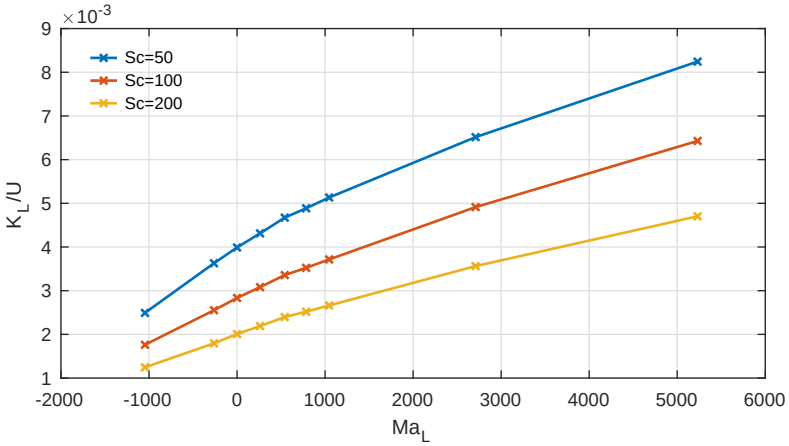

Fig. 5 Variation of K_L (at the time where K_L is maximum) a) with Ma_L for different Sc. b) with Sc for different Ma_L. The fitted slope n ($K_L \propto Sc^n$) is obtained using the data points of $Sc = 50, 100, 200$. In all simulations $Ra_L = 21200$.

Acknowledgements The simulations were performed on the supercomputer bwUniCluster 2.0 supported by the state of Baden-Württemberg, Germany through bwHPC.

References

1. R Wanninkhof, WE Asher, DT Ho, C Sweeney, and WR McGillis. Advances in quantifying air-sea gas exchange and environmental forcing. *Ann. Rev. Marine Sc.*, 1:213–244, 2009.

2. CS Garbe, A Rutgersson, J Boutin, G de Leeuw, B Delille, CW Fairall, N Gruber, J Hare, DT Ho, MT Johnson, et al. Transfer across the air-sea interface. *Ocean-Atmosphere Interactions of Gases and Particles*, pages 55–112, 2014.
3. A Rutgersson and A Smedman. Enhanced air–sea CO2 transfer due to water-side convection. *J. Marine Systems*, 80(1-2):125–134, 2010.
4. E Podgrajsek, E Sahlée, and A Rutgersson. Diurnal cycle of lake methane flux. *J. Geophys. Research: Biogeosciences*, 119(3):236–248, 2014.
5. S MacIntyre, AT Crowe, A Cortés, and L Arneborg. Turbulence in a small arctic pond. *Limnology and Oceanography*, 63(6):2337–2358, 2018.
6. WG Spangenberg and WR Rowland. Convective circulation in water induced by evaporative cooling. *Phys. Fluids*, 4(6):743–750, 1961.
7. JA Maroto, V Pérez-Munuzuri, and MS Romero-Cano. Introductory analysis of Bénard–Marangoni convection. *Eur. J. of physics*, 28(2):311, 2007.
8. JG Wissink and H Herlina. Direct numerical simulation of gas transfer across the air–water interface driven by buoyant convection. *J. Fluid Mech.*, 787:508–540, 2016.
9. JRA Pearson. On convection cells induced by surface tension. *J. Fluid Mech.*, 4(5):489–500, 1958.
10. S Chandrasekhar. *Hydrodynamic and hydromagnetic stability*. Courier Corporation, 2013.
11. E Bodenschatz, W Pesch, and G Ahlers. Recent developments in rayleigh-bénard convection. *Ann. Rev. Fluid Mech.*, 32(1):709–778, 2000.
12. A Nepomnyashchy, JC Legros, and I Simanovskii. *Interfacial convection in multilayer systems*. Springer, 2006.
13. DA Nield. Surface tension and buoyancy effects in cellular convection. *J. Fluid Mech.*, 19(3):341–352, 1964.
14. G Toussaint, H Bodiguel, F Doumenc, B Guerrier, and C Allain. Experimental characterization of buoyancy-and surface tension-driven convection during the drying of a polymer solution. *Int. J. Heat and Mass Transfer*, 51(17-18):4228–4237, 2008.
15. RA Handler, JR Saylor, RI Leighton, and AL Rovelstad. Transport of a passive scalar at a shear-free boundary in fully developed turbulent open channel flow. *Phys. Fluids*, 11(9):2607–2625, 1999.
16. ST Fredriksson, L Arneborg, H Nilsson, Q Zhang, and RA Handler. An evaluation of gas transfer velocity parameterizations during natural convection using DNS. *J. Geophys. Research: Oceans*, 121(2):1400–1423, 2016.
17. HR Khakpour, L Shen, and DKP Yue. Transport of passive scalar in turbulent shear flow under a clean or surfactant-contaminated free surface. *J. Fluid Mech.*, 670:527–557, 2011.
18. JG Wissink, H Herlina, Y Akar, and M Uhlmann. Effect of surface contamination on interfacial mass transfer rate. *J. Fluid Mech.*, 830:5–34, 2017.
19. JG Wissink and H Herlina. Surface-temperature-induced Marangoni effects on developing buoyancy-driven flow. *J. Fluid Mech.*, 962:A23, 2023.